

Article

Antimicrobial Cu-Doped TiO₂ Coatings on the β Ti-30Nb-5Mo Alloy by Micro-Arc Oxidation

Giovana Collombaro Cardoso ^{1,2,*}, Katia Barbaro ³, Pedro Akira Bazaglia Kuroda ¹, Angela De Bonis ⁴, Roberto Teghil ⁴, Ivan I. Krasnyuk, Jr. ⁵, Luca Imperatori ², Carlos Roberto Grandini ¹ and Julietta V. Rau ^{2,5}

- ¹ Laboratório de Anelasticidade e Biomateriais, UNESP—Universidade Estadual Paulista, Bauru 17033-360, SP, Brazil; pedro.kuroda@unesp.br (P.A.B.K.); carlos.r.grandini@unesp.br (C.R.G.)
- ² Istituto di Struttura della Materia, Consiglio Nazionale delle Ricerche (ISM-CNR), Via del Fosso del Cavaliere 100, 00133 Rome, Italy; luca.imperatori@cnr.it (L.I.); giulietta.rau@ism.cnr.it (J.V.R.)
- ³ Istituto Zooprofilattico Sperimentale Lazio e Toscana “M. Aleandri”, Via Appia Nuova 1411, 00178 Rome, Italy; katia.barbaro@izslt.it
- ⁴ Dipartimento di Scienze, Università della Basilicata, Via dell’Ateneo Lucano 10, 85100 Potenza, Italy; angela.debonis@unibas.it (A.D.B.); roberto.teghil@unibas.it (R.T.)
- ⁵ Department of Analytical, Physical and Colloid Chemistry, Institute of Pharmacy, Sechenov First Moscow State Medical University, Trubetskaya 8, Build. 2, 119048 Moscow, Russia; krasnyuk_i_i_1@staff.sechenov.ru
- * Correspondence: giovana.collombaro@unesp.br

Abstract: Among the different surface modification techniques, micro-arc oxidation (MAO) is explored for its ability to enhance the surface properties of Ti alloys by creating a controlled and durable oxide layer. The incorporation of Cu ions during the MAO process introduces additional functionalities to the surface, offering improved corrosion resistance and antimicrobial activity. In this study, the β -metastable Ti-30Nb-5Mo alloy was oxidated through the MAO method to create a Cu-doped TiO₂ coating. The quantity of Cu ions in the electrolyte was changed (1.5, 2.5, and 3.5 mMol) to develop coatings with different Cu concentrations. X-ray diffraction, X-ray photoelectron spectroscopy, scanning electron and atomic force microscopies, contact angle, and Vickers microhardness techniques were applied to characterize the deposited coatings. Cu incorporation increased the antimicrobial activity of the coatings, inhibiting the growth of *Staphylococcus aureus*, *Enterococcus faecalis*, *Pseudomonas aeruginosa* bacteria strains, and *Candida albicans* fungus by approximately 44%, 37%, 19%, and 41%, respectively. Meanwhile, the presence of Cu did not inhibit the growth of *Escherichia coli*. The hardness of all the deposited coatings was between 4 and 5 GPa. All the coatings were non-cytotoxic for adipose tissue-derived mesenchymal stem cells (AMSC), promoting approximately 90% of cell growth and not affecting the AMSC differentiation into the osteogenic lineage.

Keywords: antimicrobial; antibacterial; micro-arc oxidation; copper; coating; surface modification; titanium alloy



Citation: Cardoso, G.C.; Barbaro, K.; Kuroda, P.A.B.; De Bonis, A.; Teghil, R.; Krasnyuk, I.I., Jr.; Imperatori, L.; Grandini, C.R.; Rau, J.V. Antimicrobial Cu-Doped TiO₂ Coatings on the β Ti-30Nb-5Mo Alloy by Micro-Arc Oxidation. *Materials* **2024**, *17*, 156. <https://doi.org/10.3390/ma17010156>

Academic Editor: Csaba Balázs

Received: 28 November 2023

Revised: 23 December 2023

Accepted: 26 December 2023

Published: 27 December 2023



Copyright: © 2023 by the authors. Licensee MDPI, Basel, Switzerland. This article is an open access article distributed under the terms and conditions of the Creative Commons Attribution (CC BY) license (<https://creativecommons.org/licenses/by/4.0/>).

1. Introduction

Titanium (Ti) and its alloys are widely studied in the biomaterials field, mainly for producing dental and orthopedic implants. Ti is a transition metal that can form solid solutions with other elements with similar atomic sizes [1]. At temperatures up to 883 °C, it has a hexagonal closest-packed (hcp) crystal structure, known as the α phase. Above this temperature, a phase transition occurs, and it has a body-centered cubic (bcc) structure known as the β phase [2]. Depending on the alloying element used, the transition temperature (β -transus) can increase (α -stabilizing elements) or decrease (β -stabilizing elements) [3].

It is known that the best elastic modulus values are found in metastable β -type alloys, thus avoiding the stress-shielding effect caused by the mechanical incompatibility between

the implant and the bone [4]. Therefore, using β -stabilizing alloy elements, such as Mo, Nb, and Ta, is preferable to develop Ti alloys with mechanical properties more suitable for use as implant biomaterials [5–10].

The Ti-30Nb-5Mo alloy, a newly developed β -metastable alloy [11,12], is more wear-resistant due to its higher hardness compared to the commercially pure Ti (CP-Ti), and it contains niobium (Nb), which can naturally form a protective layer of TiO_2 and Nb_2O_5 , thereby enhancing its corrosion resistance [13,14]. The alloy has an elastic modulus (69 GPa) closer to that of human bone, reducing the “stress shielding” effect [2].

However, even with the excellent properties that Ti alloys present, there is still a lack of bioactivity on their surface. In this way, the functionalization of the surface of the alloys is sought to be imparted by different methods [15]. One of the most straightforward and versatile one is the micro-arc oxidation (MAO) technique, also called plasma electrolytic oxidation (PEO) [16–18].

Surface treatment via the MAO technique allows the production of a thin porous layer with different properties, which protects the substrate (alloy) from corrosion and wear and reduces the release of potentially harmful ions from the alloy [19,20]. Furthermore, it also allows the incorporation of essential ions to promote cell adhesion and osseointegration and provides antimicrobial activity [18,21].

The elements most incorporated into coatings to obtain antimicrobial activity are silver (Ag), copper (Cu), and zinc (Zn) [22–26]. Among these elements, it has already been reported that materials incorporated with Cu also exhibit higher cytocompatibility [27]. Furthermore, the presence of Cu in biomaterials can improve angiogenic and osteogenic activities [28]. By interfering with DNA replication and causing disruption of the cell membrane of both Gram-positive and Gram-negative bacteria, Cu has excellent antibacterial properties [29–31]. In the literature, there are still no reports about the production of MAO coatings on the Ti-30Nb-5Mo alloy containing Cu as a bactericidal agent.

In the current study, TiO_2 MAO coatings incorporating Mg are generated to enhance the biocompatibility of Ti alloys for orthopedic applications [32,33]. Magnesium (Mg) is a biocompatible metal that exhibits a natural affinity with biological tissues. This property reduces the probability of rejection or adverse reactions within the body [34].

This study aimed to investigate the influence of different concentrations of Cu in the TiO_2 MAO coating on the Ti-30Nb-5Mo alloy. The coatings' physicochemical properties were evaluated via X-ray diffraction (XRD), X-ray photoelectron spectroscopy (XPS), scanning electron microscopy (SEM), atomic force microscopy (AFM), contact angle, and Vickers microhardness measurements. The microbiology tests were carried out with *Escherichia coli* (*E. coli*), *Staphylococcus aureus* (*S. aureus*), *Enterococcus faecalis* (*E. faecalis*), *Pseudomonas aeruginosa* (*P. aeruginosa*) bacterial strains, and *Candida albicans* (*C. albicans*) fungus. The growth and differentiation of adipose tissue-derived mesenchymal stem cells (AMSC) were verified through MTT and alizarin red S.

2. Materials and Methods

The Ti-30Nb-5Mo alloy used as substrate was produced by arc-melting with a non-consumable tungsten electrode in a copper crucible. The crucible was cooled with running water inside an argon-controlled atmosphere furnace during the entire melting process. After melting, the ingots were hot-rolled and cut into square samples measuring $10 \times 10 \times 1 \text{ mm}^3$. Then, the samples were heat-treated at $1000 \text{ }^\circ\text{C}$ for 6 h, with a heating and cooling rate of $10 \text{ }^\circ\text{C}/\text{min}$. More information about this alloy's cast and properties can be found in the literature [11,12,35].

To carry out the MAO surface modifications, the surfaces of the alloys were sanded with 600 mesh sandpaper to standardize the roughness of the materials. A DC power source, Keysight, N5751A (Keysight, Santa Rosa, CA, USA), was utilized for the MAO process. The oxidation treatment was conducted at room temperature for 1 min, with limited current (2.5 A) and 300 V. The electrolyte solution consisted of 0.35 M calcium acetate monohydrate ($(\text{CH}_3\text{COO})_2\text{Ca}\cdot\text{H}_2\text{O}$), 0.02 M β -glycerol phosphate pentahydrate ($\text{C}_3\text{H}_7\text{Na}_2\text{O}_6\text{P}\cdot 5\text{H}_2\text{O}$),

and 0.1 M magnesium acetate tetrahydrate ($(\text{CH}_3\text{COO})_2\text{Mg}\cdot 4\text{H}_2\text{O}$) [36–39]. To incorporate Cu into the coatings, different concentrations of copper chloride (CuCl_2) were used (1.5, 2.5, and 3.5 mMol). The samples were labeled as 1.5 Cu, 2.5 Cu, and 3.5 Cu, corresponding to the different CuCl_2 concentrations.

An optical microscope, Olympus BX51 M (Olympus, Tokyo, Japan), was used to obtain cross-sectional images. In contrast, topography images were acquired using a Zeiss 300 FE scanning electron microscope (SEM) (Carl Zeiss, Oberkochen, Germany). ImageJ software (version 1.53t) was used to analyze micrographs and cross-sectional images, enabling the acquisition of pore size and thickness information.

XRD results were acquired using a MiniFlex600 diffractometer (Rigaku, Tokyo, Japan) with $\text{Cu K}\alpha$ radiation. Data was collected with $10^\circ/\text{min}$ collection time and 0.04° steps.

XPS data were obtained using a SPECS Phoibos 100-MCD5 spectrometer (SPECS Berlin, Germany) with $\text{Al K}\alpha$ radiation. The instrument operated in the fixed analyzer transmission mode at 100 W. Channel width was 1 eV for broad regions, while 0.1 eV was used for detailed regions.

AFM images were acquired using a Park XE-120 microscope (Park, Suwon, Korea) in non-contact mode. $30 \times 30 \mu\text{m}^2$ images were taken to estimate each surface roughness.

To determine the wettability of the samples, measurements of the contact angle with deionized water were conducted using the droplet technique on a Krüss DSHAT HTM Reetz GmbH goniometer (HTM Reetz GmbH, Berlin, Germany). Each sample was tested in three different regions.

The Jönsson and Hogmark “law-of-mixtures” model [40–43] was used to obtain the coatings and substrate hardness values. Leica VMHT equipment (Leica GmbH in Wetzlar, Germany) was used to perform the measurements. A Vickers pyramidal indenter was employed to make indentations on both the substrate and the MAO coatings for 15 s, with loads ranging from 0.98 to 19.6 N. Six indentations were made for each load on the substrates, and 10 were made for each load on the MAO coatings.

Four different bacteria strains (*E. coli*, *S. aureus*, *E. faecalis*, and *P. aeruginosa*) were used to test the growth of microorganisms on the coatings, along with one fungus (*C. albicans*). Before the tests, the samples were autoclaved for 20 min at 121°C . Then, each sample was placed in tubes with a suspension of a single microorganism in 5 mL of Brain Heart Infusion (BHI, DIFCO, Sparks, MD, USA) medium. The tests were performed in triplicate, and no samples were present in the BHI medium that served as the control. The microorganisms were cultivated at their optimal growth temperature (37°C for bacteria and 28°C for fungus) with slow agitation for 24 h. The growth of microorganisms was read via the optical density at a wavelength of 600 nm using a biophotometer (Eppendorf, Hamburg, Germany).

Adipose Mesenchymal Stem Cells (AMSCs) were obtained from the adipose tissue of 3-month-old female lambs of a local slaughterhouse for the cytotoxicity and differentiation tests. The cells were then incubated with the substrates for 24 h, and MTT solution (3-[4,5-dimethylthiazol-2-yl]-2,5-diphenyl-tetrazolium bromide, Sigma-Aldrich, Gillingham, UK) was added to the DMEM medium (Gibco, Loughborough, UK) containing 10% fetal calf serum (FCS, Gibco, Loughborough, UK). Afterwards, the cells were incubated at 37°C for 3 h with 5% CO_2 . Finally, the culture medium was removed, and the MTT solution was substituted with absolute ethanol (Sigma-Aldrich, Gillingham, UK).

To evaluate the capacity of AMSCs for osteogenic differentiation, the cells were treated with a DMEM medium containing 10% FCS supplemented with $50 \mu\text{g}/\text{mL}$ ascorbic acid, 10 mM β -glycerophosphate, and 10^{-7} M dexamethasone for three weeks. The treated AMSCs were then fixed in 70% ethanol at room temperature for 1 h and washed with distilled water. The cells were then stained with 2% alizarin red S (Carlo Erba, Cornaredo, Italy) for 30 min to detect the presence of Ca deposits, which turned orange-red.

3. Results and Discussion

The circuit's current was continuously monitored during the MAO treatment process, and Figure 1 displays the current's evolution over time. The current behavior during

the MAO treatment can be divided into galvanostatic and potentiostatic stages [44]. In the galvanostatic stage (highlighted in the blue frame of Figure 1), the current remains constant at the limit value established before the start of the process. During this period, the formation and growth of the compact oxide layer occur [45]. At this stage, the number of plasma discharges is higher due to the more elevated surface conductivity, as the ceramic coating is still growing on the surface [45,46]. The growth of the coating increases the electrical resistance of the sample, causing dielectric barrier breakdown at vulnerable points on the surface, and consequently, the decrease and subsequent stabilization of the current (potentiostatic stage) [39,45].

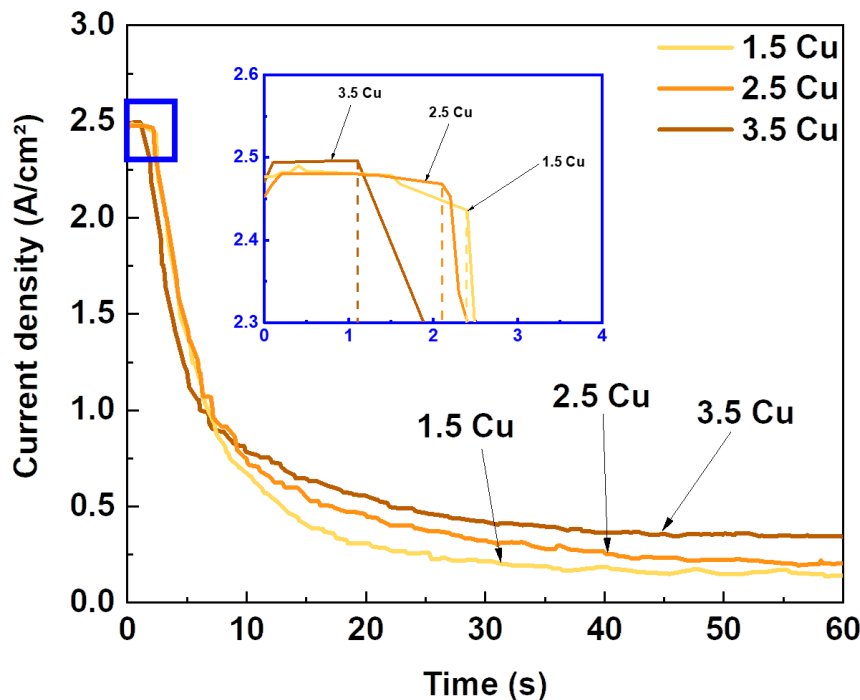


Figure 1. Current density versus time curves during the MAO process with different Cu concentrations.

Figure 1 highlights the instant in which the dielectric breakdown of the circuit occurred using the three different electrolyte solutions, and the corresponding values are presented in Table 1. It was observed that with the increase in the amount of CuCl₂, the time for the dielectric breakdown decreased. Wang et al. [47] studied the variation of NaPO₃ concentration during the MAO process and observed that the time for rupture also decreased with increasing electrolyte concentration. According to Wang et al. [47], during the constant voltage of the MAO process, the current versus time curve is directly proportional to the plasma discharge intensity. This discharge intensity is proportional to the energy of the process, thereby accelerating the dielectric breakdown process. Therefore, the increase in CuCl₂ concentration in this current study led to an increase in the conductivity of the electrolyte solution and, consequently, an increase in the energy of the MAO process.

Table 1. Dielectric breakdown time and electric charge density during the MAO process with different Cu concentrations.

Sample	Dielectric Breakdown (s)	Electric Charge Density of the Entire Process (C/cm ²)
1.5 Cu	2.4	27.3
2.5 Cu	2.1	32.6
3.5 Cu	1.1	36.7

To verify the increase in process energy, the amount of electrical charge from the treatments of each sample was calculated, and the result is presented in Table 1. Since

current (i) can be described as the rate at which the electrical charge (q) passes through a point or region (Equation (1)) [48], the electrical charge of each process can be calculated by determining the area under each curve shown in Figure 1. Thus, it is observed that the increase in CuCl_2 in the electrolyte increased the circuit charge.

$$i = \frac{dq}{dt} \quad (1)$$

Figure 2 shows SEM images of the coatings' topography and optical microscopy images of sample cross-sections after the MAO process. All coatings produced on the Ti-30Nb-5Mo alloy presented a typical morphology of MAO coatings on Ti alloys: rough surface formed by numerous pores in the shape of craters and volcanoes. This typical topography is due to the dielectric breakdown that occurs during the MAO process, which produces bubbles in the contact region between the sample surface and the electrolyte [49]. It was also observed that the increase in electrical charge led to the appearance of cracks on the surface of the coatings. The 1.5 Cu sample shows no cracks, while the 2.5 Cu sample showed some tiny cracks, as indicated in Figure 2d. Finally, in the 3.5 Cu sample, larger cracks can be seen (Figure 2g). Yao et al. [23] studied the incorporation of Cu into Ti alloys. They also observed the appearance of cracks in the coating formed due to the release of stresses generated during the MAO process. The appearance of cracks in the coatings may seem like an adverse effect. However, according to Yao et al. [23], the cracks and the pores can serve as Cu deposition channels in the inner layers of the coating. Thus, the Cu can be preserved longer if the material is applied to implants for extended periods.

Analyzing the SEM images at high magnification (Figure 2b,e,h), the more Cu was used in the MAO process, the more particles deposited on the coatings' surface were observed. Yao et al. [23] and Zhang et al. [28] also observed nanoparticle accumulation on Cu-doped TiO_2 coatings. The accumulation of these particles can be caused by increasing the temperature of the MAO process when higher amounts of Cu are added to the electrolyte [50].

The pore size of each surface was calculated using ImageJ software from the SEM images. The results are presented in Figure 3 as a histogram of the pore area. In all coatings, most pores are up to $0.25 \mu\text{m}^2$, with some larger pores up to $8 \mu\text{m}^2$. To have a better estimation of the pore size of each coating, the ratio (s/T) of the number of pores up to $0.25 \mu\text{m}^2$ (s) was determined concerning the total number of pores (T). Thus, the higher the s/T ratio is, the smaller the coating pores are. The result of the s/T ratio is presented in Figure 4 together with the thickness of each coating also determined with ImageJ software. It is observed that the more Cu was used in the electrolyte, the higher the s/T ratio was, i.e., the smaller the pores produced in the coating are.

Regarding the thickness, analysis of the samples' cross-section showed that the Cu variation was insufficient to modify the coatings' thickness. The same result was observed by Zhang et al. [51], who studied the variation of Cu in the electrolyte for CP-Ti oxidation and found that the thickness of all coatings was approximately the same size.

Figure 5 presents the XRD patterns obtained for each of the MAO coatings. All the coatings only exhibited diffraction peaks corresponding to the anatase and rutile phases of TiO_2 , except for the 3.5 Cu sample, which also showed a calcium phosphate peak. Due to the low Cu concentration, no Cu-containing phases were detected [28]. Using Equation (2) [52], it was possible to calculate the proportion of each phase, and the results are presented in Figure 6. The intensities of each peak in the diffractogram were considered to calculate the percentage of each phase. The results showed no significant variations between the percentages of anatase and rutile phases of TiO_2 . Several other studies that also incorporated Cu into MAO coatings on Ti varying Cu concentrations did not report any changes in the XRD phase composition [23,51,53,54].

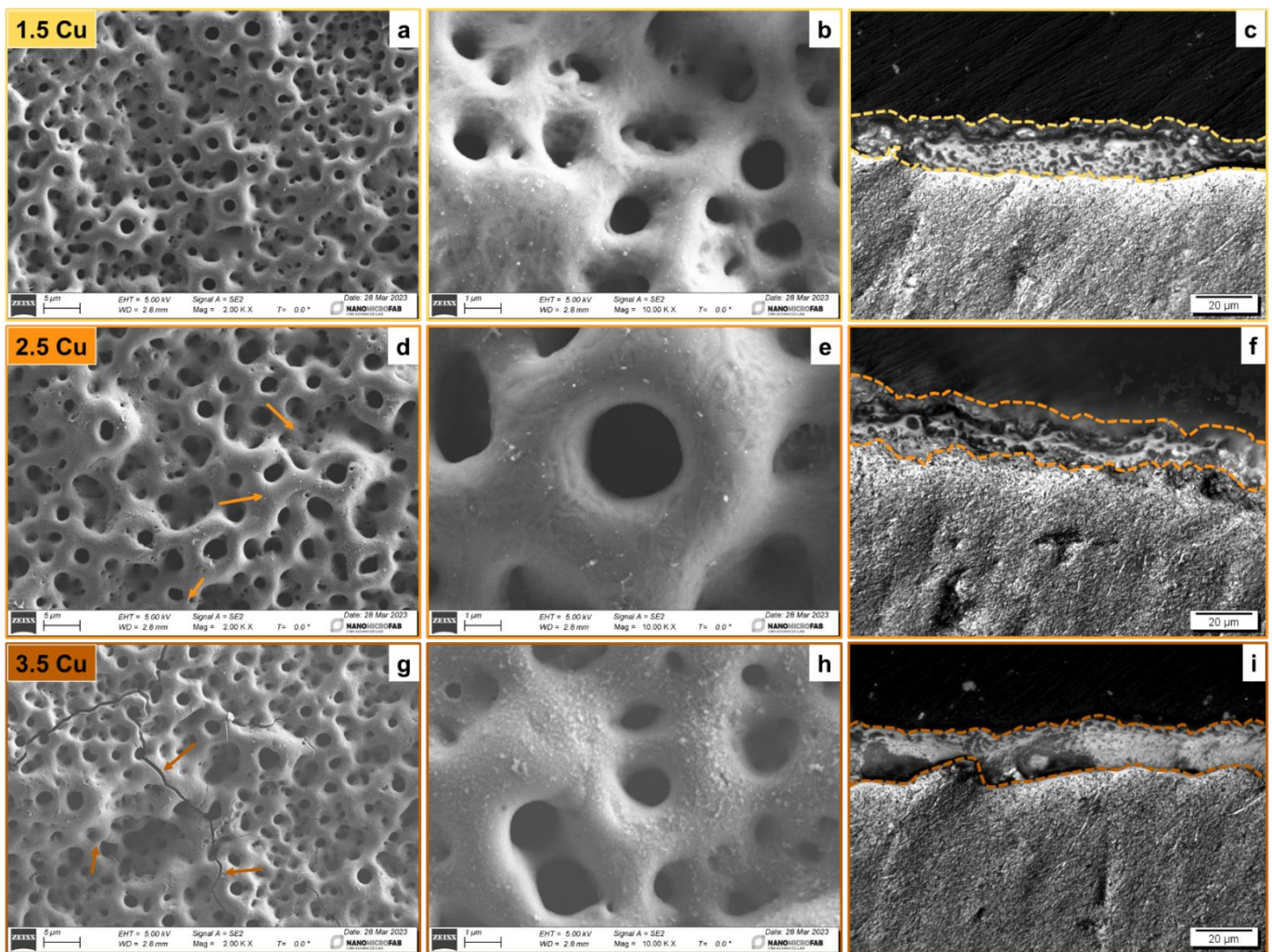


Figure 2. SEM images at $2k\times$ (a,d,g) and $10k\times$ (b,e,h) magnifications, and cross-sectional images (c,f,i) of the 1.5 Cu (a–c), 2.5 Cu (d–f), and 3.5 Cu (g–i) samples.

Standards were taken from the American Mineralogist Crystal Structure Database: β -Ti (0013128), anatase (0019093), rutile (0001737), and calcium phosphate (0020245).

$$\%phase = \frac{\sum I_{phase}}{\sum I_{all\ phase}} \quad (2)$$

Figure 7 shows the high-resolution XPS spectra of the alloying elements incorporated into the coating. Regarding the alloying elements, doublets related to TiO_2 (Figure 7a) and Nb_2O_5 (Figure 7b) were observed at 458.5 and 464.1 eV [38,44,55–57] and 207.1 e 209.8 eV [44], respectively. Mo is present in low quantities in the alloy (5% by weight) and is also known as a valve metal. Because of this, the oxidation of Mo through the MAO method is less favorable from an energetic point of view [58,59]. Consequently, no peaks of this element were detected (Figure 7c). Regarding the Cu incorporated into the coating by the MAO process, doublets of Cu_2O at 933.2 and 952.0 eV, and CuO at 935.7 and 955.8 eV were detected (Figure 7d) [54,60,61]. Lastly, in the $O1s$ spectrum (Figure 7e), peaks of metallic oxides at 530.8 eV and hydroxide (OH) at 531.8 eV [56,62] were registered. Analyzing the composition of each Cu oxide, it was observed that there was an increase in the CuO/Cu_2O ratio (0.15, 0.21, and 0.37) as the Cu concentration in the electrolyte increased. Yang et al. [61] reported the same effect when increasing Cu incorporation in CP-Ti samples. The following redox reactions occur during the MAO process to form CuO and Cu_2O [60]. Thus, with

more CuCl₂ available in the electrolyte, the redux reaction of 2Cu₂O into 4CuO occurs, increasing the CuO/Cu₂O ratio.

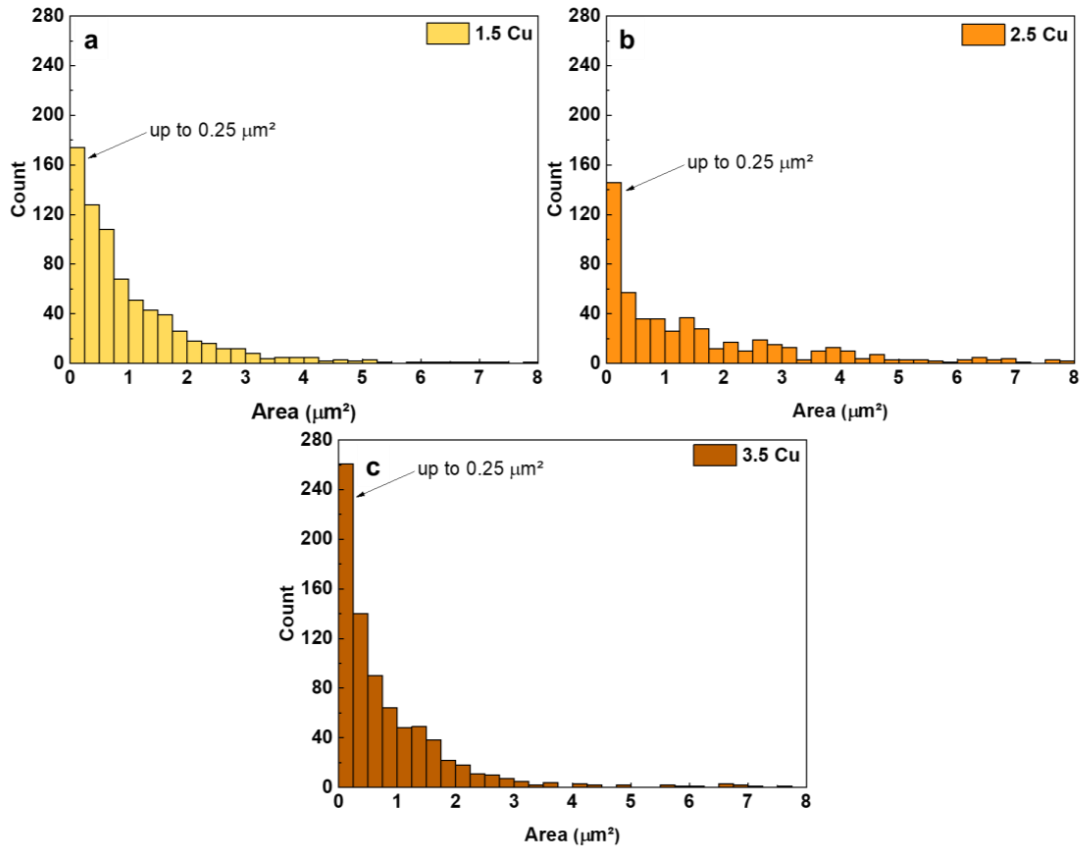
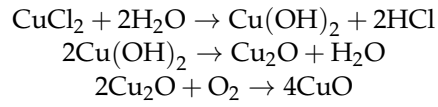


Figure 3. Pore area histograms of the 1.5 Cu (a), 2.5 Cu (b), and 3.5 Cu (c) samples.

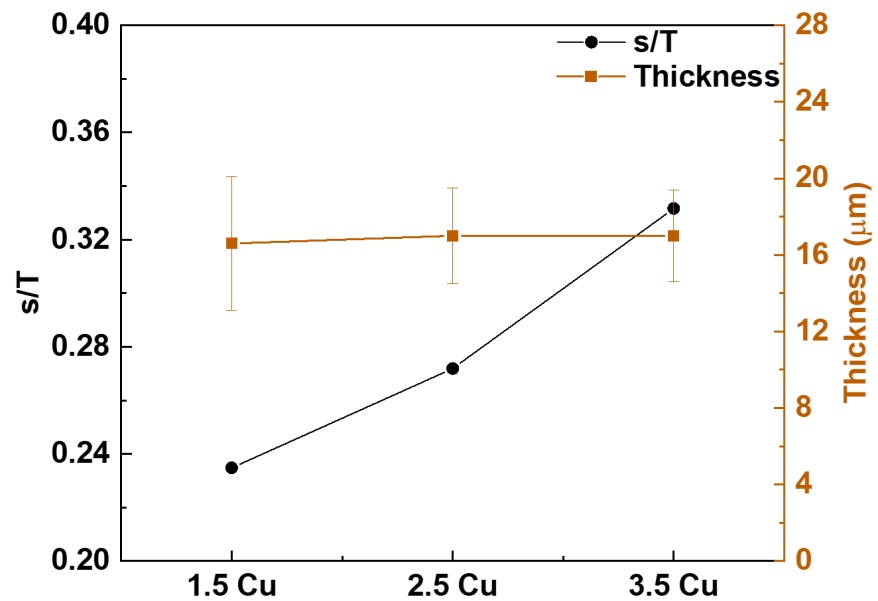


Figure 4. S/T ratio and thickness of the MAO coatings with different Cu concentrations.

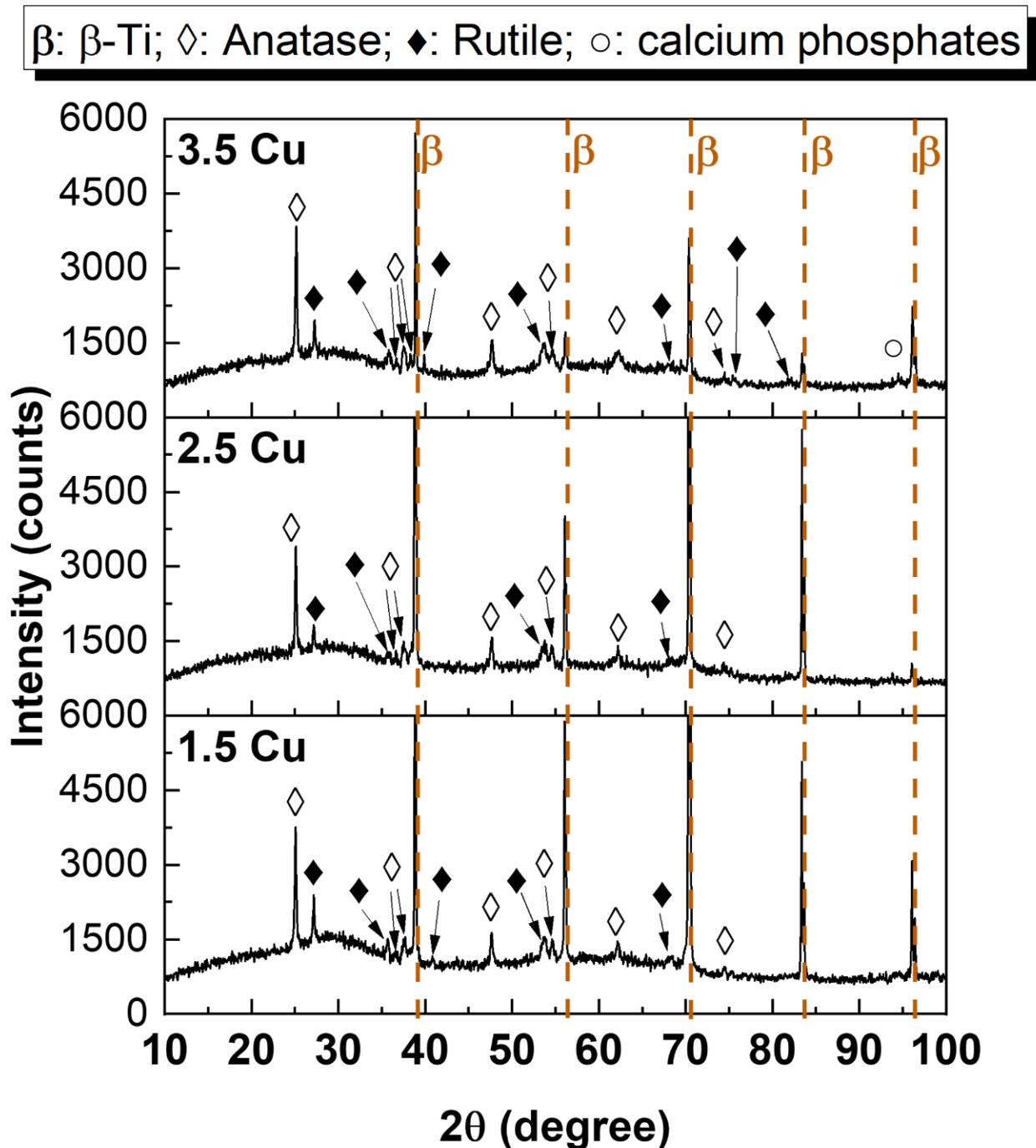


Figure 5. XRD patterns of the MAO coatings with different Cu concentrations.

Figure 8 shows the composition of the elements identified by XPS. It was observed that with an increase in Cu concentration in the electrolyte, the concentration of all elements, except for C and Ca, grew due to the increase in electrolyte conductivity. Kuroda et al. [63] explained that the energy of the process influences the flow of electrons through the coating produced by the MAO method, so higher electrical conductivity increases the rate of ions reaching the coating.

The 3D topographic images of the coating surfaces obtained by the AFM technique are presented in Figure 9. From these images, it was possible to determine the average surface roughness (RMS), and the results are presented in Figure 10 (blue line), along with the contact angle values with distilled water (bars). It was observed that the variation of

CuCl_2 in the electrolyte did not significantly change the coatings' roughness and contact angle values. Wang et al. [54], who studied the effect of Cu on the production of MAO coatings on CP-Ti, also obtained similar results: there were no significant changes in the roughness and wettability of the surfaces.

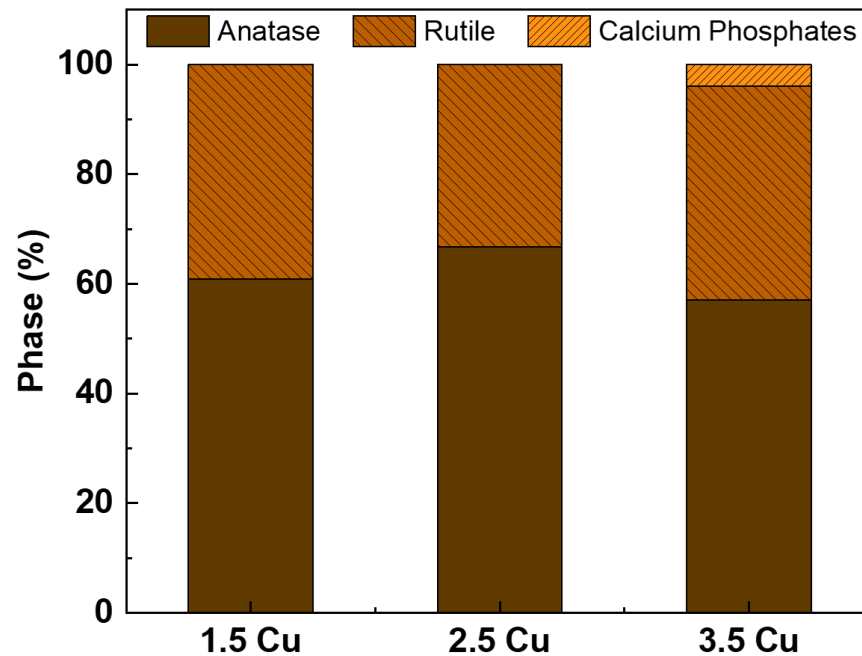


Figure 6. Phase composition by XRD and crystallinity of the MAO coatings with different Cu concentrations.

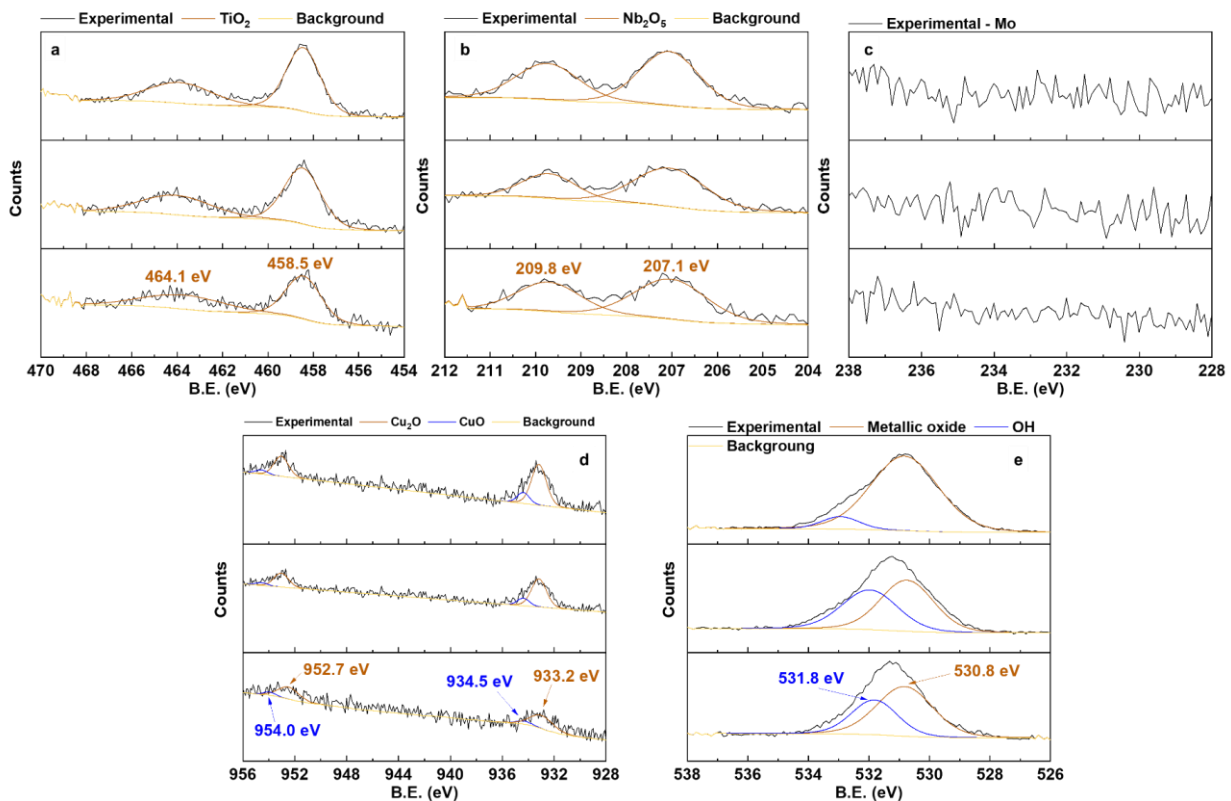


Figure 7. High-resolution XPS of the Ti (a), Nb (b), Mo (c), Cu (d), and O (e) present in the MAO coatings.

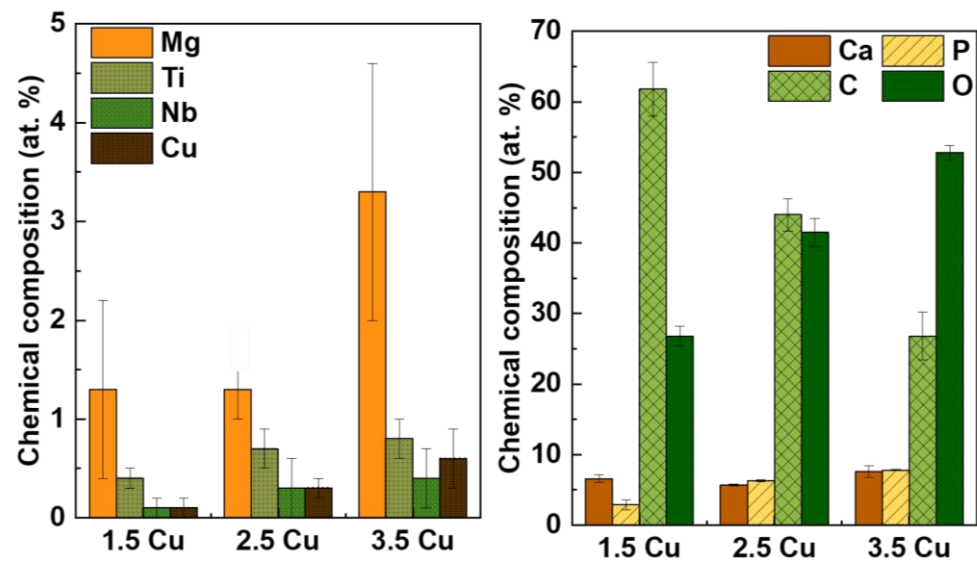


Figure 8. Chemical composition obtained by XPS of the MAO coatings.

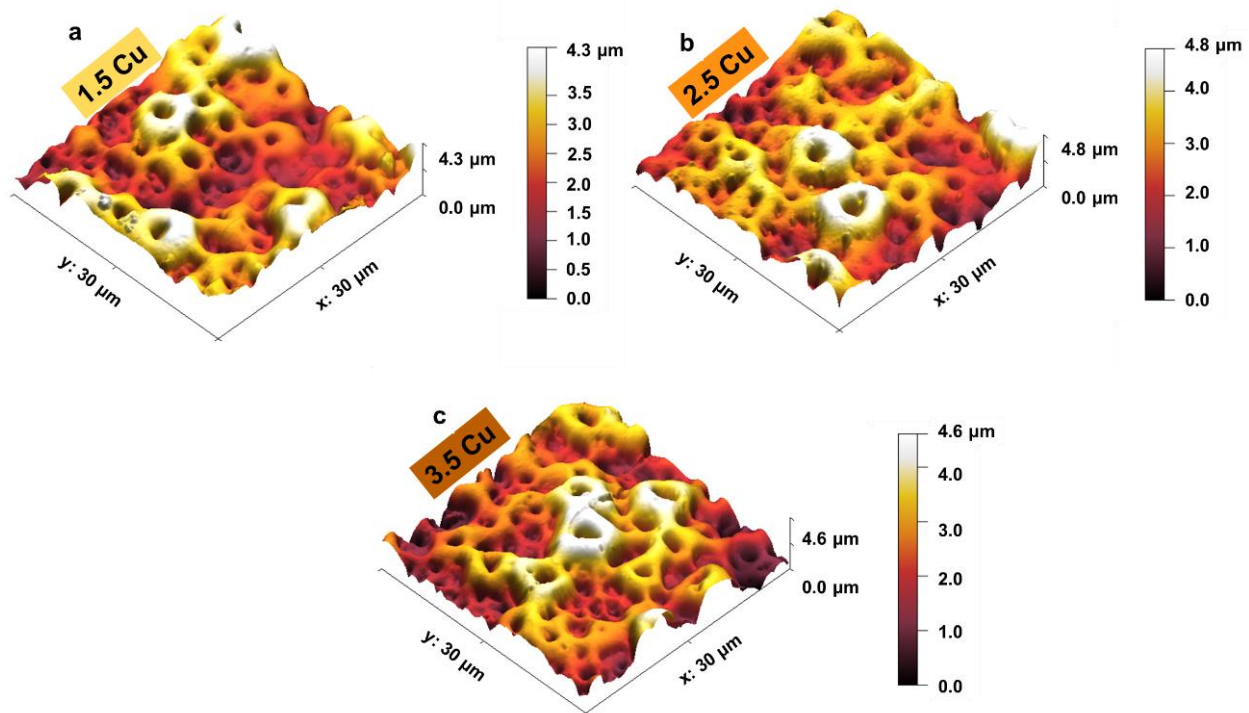


Figure 9. Three-dimensional topography images of the 1.5 Cu (a), 2.5 Cu (b), and 3.5 Cu (c) samples.

Although all coatings produced on the Ti-30Nb-5Mo alloy substrates show no considerable variations in contact angle, their values are below 90° , indicating the hydrophilicity of the coatings. This situation is because TiO_2 , the main component of the coatings, has a high surface polarity, making it more susceptible to bonding with water molecules [39,62,64].

The hardness of the substrate and coatings after each MAO process with different electrolyte solutions are shown in Figure 11. The different electrolytes did not considerably change the substrate's hardness, which varied between 2.5 and 2.8 GPa. The values obtained are similar to those reported by Cardoso et al. [11] (2.8 ± 0.1 GPa), who studied the mechanical properties of the Ti-30Nb-5Mo alloy.

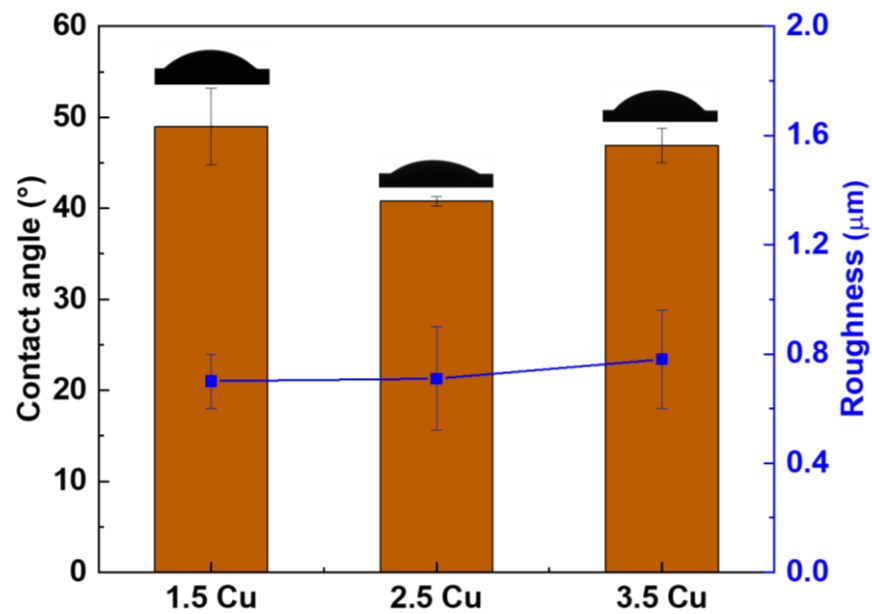


Figure 10. Contact angle and surface roughness of the MAO coatings with different Cu concentrations.

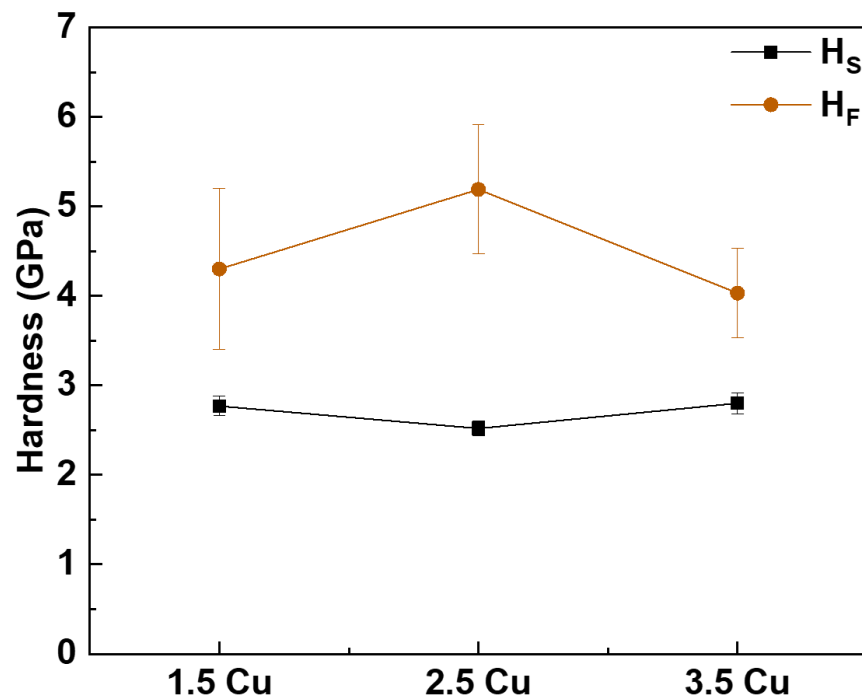


Figure 11. Hardness of the substrates (H_s) and the MAO coatings (H_f) with different Cu concentrations.

It was not possible to observe any trend in the variation of coating hardness with increasing Cu content. The hardness of the 1.5 Cu coating was 4.3 ± 0.9 GPa. This value increased to 5.2 ± 0.7 GPa for the 2.5 Cu sample and decreased again to 4.0 ± 0.5 GPa for the sample with the highest Cu concentration (3.5 Cu). The slight variation in hardness values can be explained by the low variation in Cu concentration between the different coatings. However, all values obtained are not very different from the values found in the literature for porous TiO_2 MAO coatings on Ti alloys (1.4 GPa [41], 2.2 GPa [65], 2.9 GPa [66], and 3.9 GPa [33]). The coatings' higher hardness values are important because they provide greater strength to the material and protect the substrate from wear [67,68].

Figure 12 shows the growth of microorganisms on the surface of different coatings incorporated with Cu. Among all the microorganisms tested, only the *E. coli* bacteria

maintained a growth rate equal to or higher than that of the control. In other words, incorporating Cu did not affect the growth of this bacteria strain. Moreover, sample 3.5 Cu showed a higher growth of *E. coli* than the control sample. This may have occurred due to the increase in the number of cracks in the coating, which provided a more favorable environment for bacteria with lower concentrations of Cu.

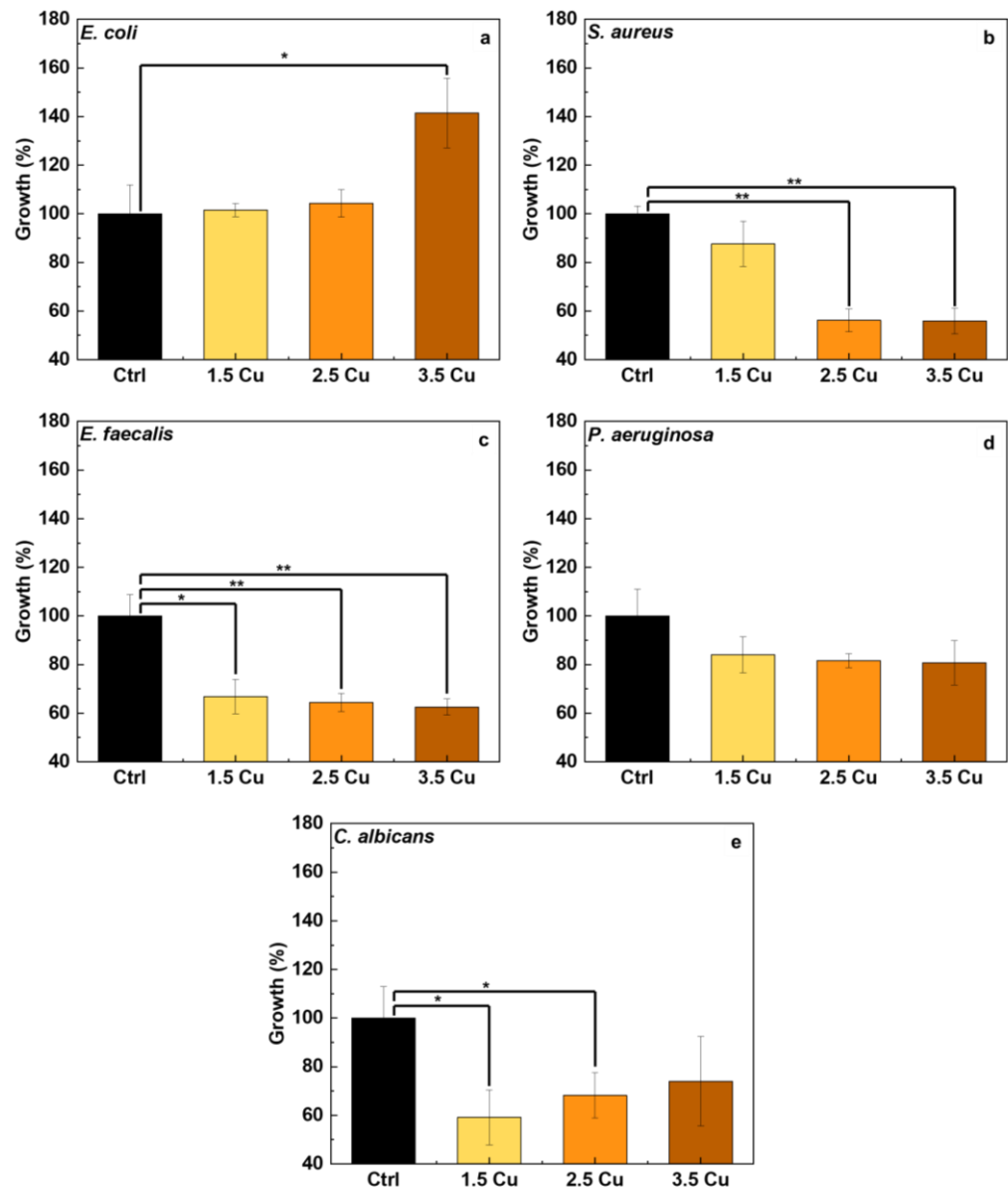


Figure 12. *E. coli* (a), *S. aureus* (b), *E. faecalis* (c), *P. aeruginosa* (d), and *C. albicans* (e) growth on the MAO coatings with different Cu concentrations. * $p < 0.05$, ** $p < 0.01$, compared with the control group.

On the other hand, the incorporation of Cu was effective in significantly reducing the growth of the bacteria strains, such as *S. aureus* (by 44%), *E. faecalis* (by 37%), and *P. aeruginosa* (by 19%), as well as the fungus *C. albicans* (by 41%). As shown in the chemical composition results obtained by XPS (Figure 8), the concentration of Cu incorporated into the coatings did not vary significantly. This may explain why Cu concentration has no apparent influence on the results obtained for *E. faecalis* and *P. aeruginosa*.

There is no consensus in the literature on the mechanisms of the bactericidal effect of Cu. Some authors attribute the effect to the absorption of Cu ions by bacteria, which leads to the formation of cavities in the bacterial cell wall [69]. In contrast, other authors suggest that there must be a significant interaction between the Cu nanoparticle and the microorganism

for contact death to occur [70]. Yao et al. [23] believe that both mechanisms (contact and release of ions) are responsible for the bactericidal effect of Cu. Shimabukuro et al. [71] studied the incorporation of Cu into CP-Ti and analyzed the bactericidal effect of the coating against *E. coli* and *S. aureus*. According to the authors [71], the effectiveness of Cu is more prominent against *S. aureus* than *E. coli*, requiring a higher minimum inhibitory concentration (MIC) of Cu to inhibit *E. coli* growth. Furthermore, the authors [71] found that the bacterial property of the coating is activated by contact with Cu, rather than through the release of ions. This situation helps to explain why there was increased growth of *E. coli* in the 3.5 Cu sample, as more bacteria colonies can form inside the cracks where there is less penetration of Cu. Furthermore, Cu₂O exhibits higher bactericidal efficiency than CuO [60], and, as shown in the XPS results of this present study, the CuO/Cu₂O ratio increased, i.e., there was more CuO on the coating surface.

The growth of AMSC cells, obtained via the MTT method, is shown in Figure 13. According to the ISO 10993-5 standard [72], up to 70% of cell viability is required for non-cytotoxicity [73–75]. Furthermore, the standard establishes that 100% cell viability samples are not cytotoxic (grade 0). Samples between 80% and 100% viability are slightly cytotoxic (grade 1). Samples with viability between 50% and 80% are mildly cytotoxic (grade 2), while samples between 30% and 50% are moderately cytotoxic (grade 3). Samples with viability below 30% are severely cytotoxic (grade 4) [72,76]. In this presented study, cell growth on all coatings was approximately 90%. Therefore, they fall into grade 1 of cytotoxicity.

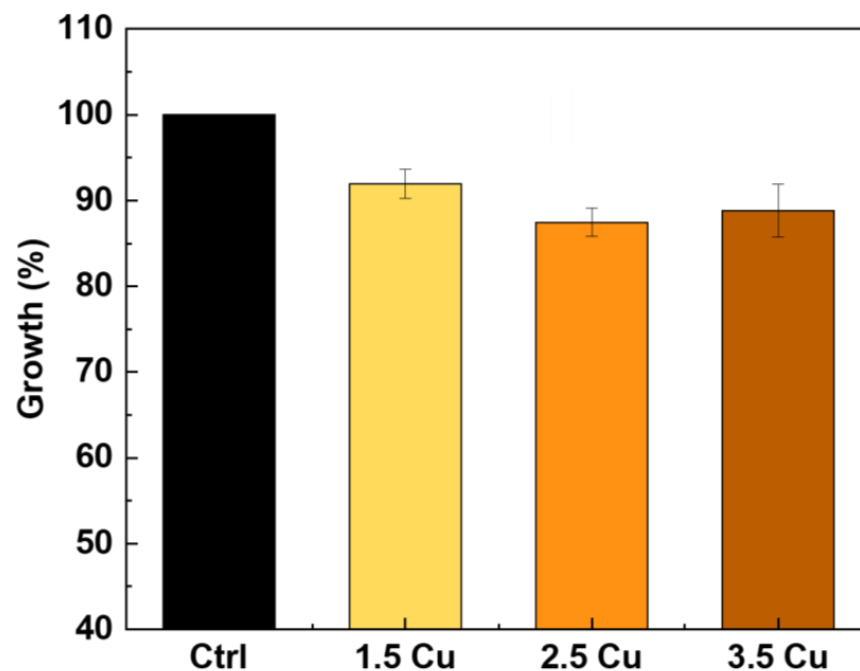


Figure 13. AMSCs growth on the MAO coatings with different Cu concentrations.

In Figure 14, the cell monolayer images of the samples with different concentrations of Cu, stained with alizarin red S to highlight in red the Ca deposits, are presented. The positive control (+Ctrl) is the AMSCs that have differentiated into the osteogenic lineage without the substrate (Figure 14a), while the negative control (-Ctrl) is represented by non-differentiated AMSCs (Figure 14b). All the samples' images resemble the positive control. Therefore, the Cu levels used did not alter the AMSCs' differentiation into the osteogenic lineage. Zhu et al. [53] and Zhang et al. [60] studied the incorporation of Cu into TiO₂ coatings produced by the MAO method. They concluded that the coatings promoted the differentiation of MG63 [53] and MC3T3-E1 [60] cells. This phenomenon occurred because the coatings are porous and provide a higher contact area with the medium used. This, in turn, can facilitate the adsorption of proteins that promote cell differentiation [60]. Furthermore, it has been reported that the expression of insulin-like

growth factor—1 (IGF-1, which plays an essential role in the growth and development of osteoblasts) is increased by Cu [53].

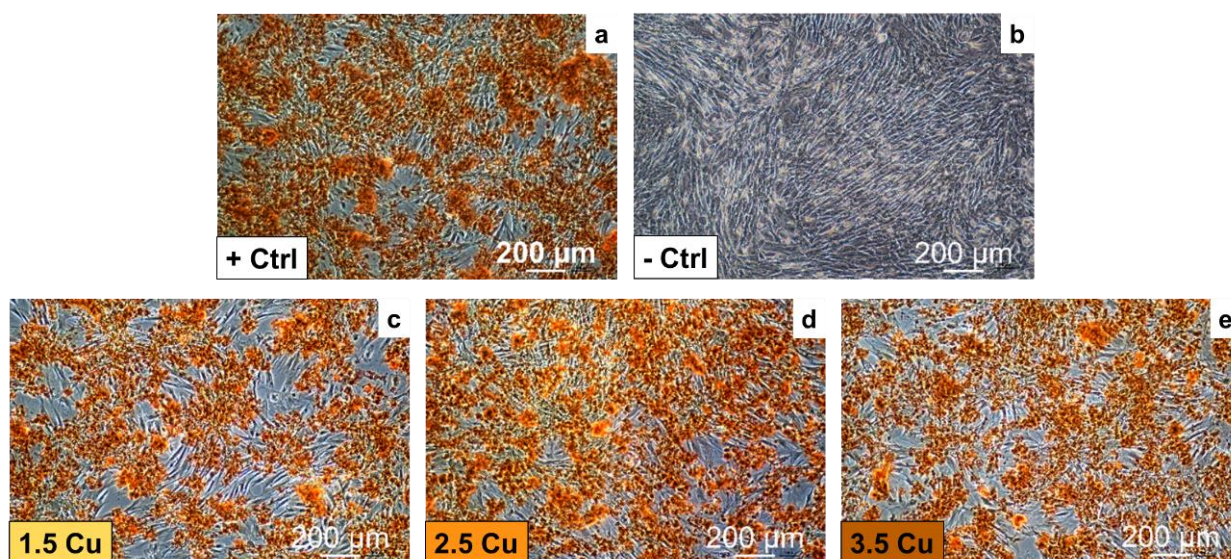


Figure 14. Alizarin red S staining of AMSCs differentiated in vitro into the osteogenic lineage on positive control (a), negative control (b), and on 1.5 Cu (c), 2.5 Cu (d), and 3.5 Cu (e) coating samples.

4. Conclusions

With the results obtained in this study, it was possible to verify how the increase in Cu ions (from 1.5 to 3.5 mMol) in the electrolyte used in the MAO process of the Ti-30Nb-5Mo alloy influenced the morphology and properties of the coatings. The XRD patterns showed that the crystalline part of the coatings comprises TiO₂ (anatase and rutile phases). A small amount of calcium phosphate (~4%) was detected in the sample with the highest Cu concentration. It was found via XPS that the CuO/Cu₂O ratio in the coatings increased from 0.15 to 0.37 due to Cu incorporation. The coating samples showed no significant variations in roughness (~0.7 to 0.8 µm) and wettability (~40 to 50°). All the coatings were hydrophilic (<90°). The hardness of the coatings also did not show significant variations, the values remaining higher (~4 to 5 GPa) compared to the substrate hardness (2.8 GPa). The incorporation of Cu into the coatings improved the antimicrobial activity of the surface since the growth of *S. aureus*, *E. faecalis*, *P. aeruginosa*, and *C. albicans* was approximately 56%, 63%, 81%, and 59% (concerning 100% of control), respectively. However, the growth of *E. coli* was not affected by the levels of Cu incorporated into the coatings. The AMSC cell growth on all the surfaces was above 90%, proving the non-cytotoxicity of the prepared coatings. Moreover, adding Cu (up to 3.5 mMol) did not affect the differentiation of AMSCs into the osteogenic lineage.

Author Contributions: Conceptualization, G.C.C.; methodology, G.C.C., K.B., P.A.B.K., A.D.B., R.T. and I.I.K.J.; formal analysis, G.C.C., K.B., P.A.B.K., A.D.B. and R.T.; investigation, G.C.C., K.B., P.A.B.K., L.I., A.D.B. and R.T.; resources, C.R.G. and J.V.R.; data curation, G.C.C., K.B. and P.A.B.K.; writing—original draft preparation, G.C.C.; writing—review and editing, C.R.G. and J.V.R.; supervision, C.R.G. and J.V.R.; project administration, C.R.G. and J.V.R.; funding acquisition, C.R.G. and J.V.R. All authors have read and agreed to the published version of the manuscript.

Funding: This research was funded by Coordenação de Aperfeiçoamento de Pessoal de Nível Superior—Brazil (CAPES) (grant #88887.716787/2022-00) and Conselho Nacional de Desenvolvimento Científico e Tecnológico (CNPq) (Grant #314.810/2021-8). The present research was partially supported by the Italian Ministry of Health, grant codes IZS LT 02/21 RC and IZS LT 10/22 RC.

Institutional Review Board Statement: Not applicable since the adipose tissue-derived mesenchymal stem cells were isolated from the adipose tissue of 3-month-old female lambs taken from a slaughterhouse.

Informed Consent Statement: Not applicable.

Data Availability Statement: The obtained data are available upon a reasonable request to the corresponding author.

Acknowledgments: The authors thank Felelon Martinho Lima Pontes for the XRD measurements. The technical support of Massimo Di Menno Di Bucchianico and Marco Ortenzi is gratefully acknowledged.

Conflicts of Interest: The authors declare no conflict of interest.

References

1. Nicholson, J.W. Titanium Alloys for Dental Implants: A Review. *Prosthesis* **2020**, *2*, 100–116. [[CrossRef](#)]
2. Niinomi, M.; Nakai, M. Titanium-Based Biomaterials for Preventing Stress Shielding between Implant Devices and Bone. *Int. J. Biomater.* **2011**, *2011*, 836587. [[CrossRef](#)] [[PubMed](#)]
3. Koizumi, H.; Takeuchi, Y.; Imai, H.; Kawai, T.; Yoneyama, T. Application of titanium and titanium alloys to fixed dental prostheses. *J. Prosthodont. Res.* **2019**, *63*, 266–270. [[CrossRef](#)] [[PubMed](#)]
4. Chen, L.-Y.; Cui, Y.-W.; Zhang, L.-C. Recent Development in Beta Titanium Alloys for Biomedical Applications. *Metals* **2020**, *10*, 1139. [[CrossRef](#)]
5. Babilas, D.; Urbańczyk, E.; Sowa, M.; Maciej, A.; Korotin, D.M.; Zhidkov, I.S.; Basiaga, M.; Krok-Borkowicz, M.; Szyk-Warszyńska, L.; Pamuła, E.; et al. On the electropolishing and anodic oxidation of Ti-15Mo alloy. *Electrochim. Acta* **2016**, *205*, 256–265. [[CrossRef](#)]
6. Inaekyan, K.; Brailovski, V.; Prokoshkin, S.; Pushin, V.; Dubinskiy, S.; Sheremetyev, V. Comparative study of structure formation and mechanical behavior of age-hardened Ti-Nb-Zr and Ti-Nb-Ta shape memory alloys. *Mater. Charact.* **2015**, *103*, 65–74. [[CrossRef](#)]
7. Hussein, A.H.; Gepreel, M.A.H.; Gouda, M.K.; Hefnawy, A.M.; Kandil, S.H. Biocompatibility of new Ti-Nb-Ta base alloys. *Mater. Sci. Eng. C* **2016**, *61*, 574–578. [[CrossRef](#)]
8. Wang, J.C.; Liu, Y.J.; Qin, P.; Liang, S.X.; Sercombe, T.B.; Zhang, L.C. Selective laser melting of Ti-35Nb composite from elemental powder mixture: Microstructure, mechanical behavior and corrosion behavior. *Mater. Sci. Eng. A* **2019**, *760*, 214–224. [[CrossRef](#)]
9. Karre, R.; Niranjana, M.K.; Dey, S.R. First principles theoretical investigations of low Young's modulus beta Ti-Nb and Ti-Nb-Zr alloys compositions for biomedical applications. *Mater. Sci. Eng. C* **2015**, *50*, 52–58. [[CrossRef](#)]
10. Verissimo, N.C.; Figueiredo, R.S.; de Oliveira, H.G.; Rodrigues, C.A.; Caram, R.; Bertazzoli, R. Characterization of the photoactivity of nanotube layers grown on Ti-35Nb and Ti-35Nb-4Sn alloys. *J. Mater. Sci.* **2016**, *51*, 9384–9393. [[CrossRef](#)]
11. Cardoso, G.C.; Kuroda, P.A.B.; Grandini, C.R. Influence of Nb addition on the structure, microstructure, Vickers microhardness, and Young's modulus of new β Ti-xNb-5Mo alloys system. *J. Mater. Res. Technol.* **2023**, *25*, 3061–3070. [[CrossRef](#)]
12. Cardoso, G.C.; de Almeida, G.S.; Corrêa, D.O.G.; Zambuzzi, W.F.; Buzalaf, M.A.R.; Correa, D.R.N.; Grandini, C.R. Preparation and characterization of novel as-cast Ti-Mo-Nb alloys for biomedical applications. *Sci. Rep.* **2022**, *12*, 11874. [[CrossRef](#)] [[PubMed](#)]
13. Cordeiro, J.M.; Nagay, B.E.; Ribeiro, A.L.R.; da Cruz, N.C.; Rangel, E.C.; Fais, L.M.G.; Vaz, L.G.; Barão, V.A.R. Functionalization of an experimental Ti-Nb-Zr-Ta alloy with a biomimetic coating produced by plasma electrolytic oxidation. *J. Alloys Compd.* **2019**, *770*, 1038–1048. [[CrossRef](#)]
14. Rabadia, C.D.; Liu, Y.J.; Cao, G.H.; Li, Y.H.; Zhang, C.W.; Sercombe, T.B.; Sun, H.; Zhang, L.C. High-strength β stabilized Ti-Nb-Fe-Cr alloys with large plasticity. *Mater. Sci. Eng. A* **2018**, *732*, 368–377. [[CrossRef](#)]
15. Sobolev, A.; Kossenko, A.; Borodianskiy, K. Study of the Effect of Current Pulse Frequency on Ti-6Al-4V Alloy Coating Formation by Micro Arc Oxidation. *Materials* **2019**, *12*, 3983. [[CrossRef](#)] [[PubMed](#)]
16. Hwang, M.-J.; Choi, H.-R.; Song, H.-J.; Park, Y.-J. Characterization and colorization of microarc-oxidized layers of binary titanium alloys. *J. Alloys Compd.* **2018**, *732*, 95–106. [[CrossRef](#)]
17. Saeed, E.M.; Dawood, N.M.; Hasan, S.F. Improvement corrosion resistance of Ni-Ti alloy by TiO₂ coating and hydroxyapatite/TiO₂ composite coating using micro arc oxidation process. *Mater. Today Proc.* **2021**, *42*, 2789–2796. [[CrossRef](#)]
18. Gabor, R.; Doubkova, M.; Gorosova, S.; Malanik, K.; Vandrovcova, M.; Cvrcek, L.; Drobikova, K.; Mamulova Kutlakova, K.; Bacakova, L. Preparation of highly wettable coatings on Ti-6Al-4V ELI alloy for traumatological implants using micro-arc oxidation in an alkaline electrolyte. *Sci. Rep.* **2020**, *10*, 19780. [[CrossRef](#)]
19. Hanawa, T. Metal ion release from metal implants. *Mater. Sci. Eng. C* **2004**, *24*, 745–752. [[CrossRef](#)]
20. Wang, X.; Mei, L.; Jiang, X.; Jin, M.; Xu, Y.; Li, J.; Li, X.; Meng, Z.; Zhu, J.; Wu, F. Hydroxyapatite-Coated Titanium by Micro-Arc Oxidation and Steam-Hydrothermal Treatment Promotes Osseointegration. *Front. Bioeng. Biotechnol.* **2021**, *9*, 625877. [[CrossRef](#)]
21. Santos-Coquillat, A.; Mohedano, M.; Martinez-Campos, E.; Arrabal, R.; Pardo, A.; Matykina, E. Bioactive multi-elemental PEO-coatings on titanium for dental implant applications. *Mater. Sci. Eng. C* **2019**, *97*, 738–752. [[CrossRef](#)] [[PubMed](#)]
22. Fosca, M.; Streza, A.; Antoniac, I.V.; Vadalà, G.; Rau, J.V. Ion-Doped Calcium Phosphate-Based Coatings with Antibacterial Properties. *J. Funct. Biomater.* **2023**, *14*, 250. [[CrossRef](#)] [[PubMed](#)]
23. Yao, X.; Zhang, X.; Wu, H.; Tian, L.; Ma, Y.; Tang, B. Microstructure and antibacterial properties of Cu-doped TiO₂ coating on titanium by micro-arc oxidation. *Appl. Surf. Sci.* **2014**, *292*, 944–947. [[CrossRef](#)]

24. Fadeeva, I.V.; Lazoryak, B.I.; Davidova, G.A.; Murzakhanov, F.F.; Gabbasov, B.F.; Petrakova, N.V.; Fosca, M.; Barinov, S.M.; Vadala, G.; Uskoković, V.; et al. Antibacterial and cell-friendly copper-substituted tricalcium phosphate ceramics for biomedical implant applications. *Mater. Sci. Eng. C* **2021**, *129*, 112410. [[CrossRef](#)] [[PubMed](#)]
25. Prosolov, K.A.; Khimich, M.A.; Rau, J.V.; Lychagin, D.V.; Sharkeev, Y.P. Influence of oblique angle deposition on Cu-substituted hydroxyapatite nano-roughness and morphology. *Surf. Coat. Technol.* **2020**, *394*, 125883. [[CrossRef](#)]
26. Rau, J.V.; Curcio, M.; Raucci, M.G.; Barbaro, K.; Fasolino, I.; Teghil, R.; Ambrosio, L.; De Bonis, A.; Boccaccini, A.R. Cu-Releasing Bioactive Glass Coatings and Their in Vitro Properties. *ACS Appl. Mater. Interfaces* **2019**, *11*, 5812–5820. [[CrossRef](#)]
27. Hang, R.; Gao, A.; Huang, X.; Wang, X.; Zhang, X.; Qin, L.; Tang, B. Antibacterial activity and cytocompatibility of Cu–Ti–O nanotubes. *J. Biomed. Mater. Res. Part. A* **2014**, *102*, 1850–1858. [[CrossRef](#)]
28. Zhang, X.; Li, J.; Wang, X.; Wang, Y.; Hang, R.; Huang, X.; Tang, B.; Chu, P.K. Effects of copper nanoparticles in porous TiO₂ coatings on bacterial resistance and cytocompatibility of osteoblasts and endothelial cells. *Mater. Sci. Eng. C* **2018**, *82*, 110–120. [[CrossRef](#)]
29. Zhang, X.; Huang, X.; Ma, Y.; Lin, N.; Fan, A.; Tang, B. Bactericidal behavior of Cu-containing stainless steel surfaces. *Appl. Surf. Sci.* **2012**, *258*, 10058–10063. [[CrossRef](#)]
30. Ruparelia, J.P.; Chatterjee, A.K.; Duttagupta, S.P.; Mukherji, S. Strain specificity in antimicrobial activity of silver and copper nanoparticles. *Acta Biomater.* **2008**, *4*, 707–716. [[CrossRef](#)]
31. Matsumoto, N.; Sato, K.; Yoshida, K.; Hashimoto, K.; Toda, Y. Preparation and characterization of β -tricalcium phosphate co-doped with monovalent and divalent antibacterial metal ions. *Acta Biomater.* **2009**, *5*, 3157–3164. [[CrossRef](#)] [[PubMed](#)]
32. Kuroda, P.A.B.; Montes, T.H.; Rossi, M.C.; Grandini, C.R.; Afonso, C.R.M. Unraveling crystalline phases, morphology, hardness, and adhesion of PEO anodic coatings on Ti-15Nb alloy surface. *Mater. Lett.* **2024**, *356*, 135607. [[CrossRef](#)]
33. Kuroda, P.A.B.; Grandini, C.R.; Afonso, C.R.M. Anodic MAO coating formation on Ti-25Ta alloy. *Mater. Lett.* **2024**, *354*, 135377. [[CrossRef](#)]
34. Zhang, T.; Wang, W.; Liu, J.; Wang, L.; Tang, Y.; Wang, K. A review on magnesium alloys for biomedical applications. *Front. Bioeng. Biotechnol.* **2022**, *10*, 953344. [[CrossRef](#)] [[PubMed](#)]
35. Cardoso, G.C.; Buzalaf, M.A.R.; Correa, D.R.N.; Grandini, C.R. Effect of Thermomechanical Treatments on Microstructure, Phase Composition, Vickers Microhardness, and Young’s Modulus of Ti-xNb-5Mo Alloys for Biomedical Applications. *Metals* **2022**, *12*, 788.
36. Ribeiro, A.R.; Oliveira, F.; Boldrini, L.C.; Leite, P.E.; Falagan-Lotsch, P.; Linhares, A.B.R.; Zambuzzi, W.F.; Fragneaud, B.; Campos, A.P.C.; Gouvêa, C.P.; et al. Micro-arc oxidation as a tool to develop multifunctional calcium-rich surfaces for dental implant applications. *Mater. Sci. Eng. C* **2015**, *54*, 196–206. [[CrossRef](#)] [[PubMed](#)]
37. Oliveira, F.G.; Ribeiro, A.R.; Perez, G.; Archanjo, B.S.; Gouvea, C.P.; Araújo, J.R.; Campos, A.P.C.; Kuznetsov, A.; Almeida, C.M.; Maru, M.M.; et al. Understanding growth mechanisms and tribocorrosion behaviour of porous TiO₂ anodic films containing calcium, phosphorous and magnesium. *Appl. Surf. Sci.* **2015**, *341*, 1–12. [[CrossRef](#)]
38. Sousa, T.S.P.; Costa, N.d.A.d.; Correa, D.R.N.; Rocha, L.A.; Grandini, C.R. Morphology, Crystalline Structure and Chemical Composition Of MAO Treated Ti-15Zr-Mo Surfaces Enriched with Bioactive Ions. *Mater. Res.* **2019**, *22*. [[CrossRef](#)]
39. Rossi, M.C.; dos Santos, R.F.; Kuroda, P.A.B.; Afonso, C.R.M. Characteristics of ceramic-like coatings obtained by plasma electrolyte oxidation on different Ti alloys. *Boletín Soc. Española Cerámica Vidr.* **2023**. [[CrossRef](#)]
40. Jönsson, B.; Hogmark, S. Hardness measurements of thin films. *Thin Solid. Film.* **1984**, *114*, 257–269. [[CrossRef](#)]
41. Cardoso, G.C.; Kuroda, P.A.B.; Grandini, C.R. A detailed analysis of the MAO TiO₂ coating hardness using the Jönsson and Hogmark “law-of-mixtures” model. *Mater. Lett.* **2023**, *352*, 135208. [[CrossRef](#)]
42. Rau, J.V.; Latini, A.; Teghil, R.; De Bonis, A.; Fosca, M.; Caminiti, R.; Rossi Albertini, V. Superhard Tungsten Tetraboride Films Prepared by Pulsed Laser Deposition Method. *ACS Appl. Mater. Interfaces* **2011**, *3*, 3738–3743. [[CrossRef](#)] [[PubMed](#)]
43. Ferro, D.; Barinov, S.M.; Rau, J.V.; Latini, A.; Scandurra, R.; Brunetti, B. Vickers and Knoop hardness of electron beam deposited ZrC and HfC thin films on titanium. *Surf. Coat. Technol.* **2006**, *200*, 4701–4707. [[CrossRef](#)]
44. Kuroda, P.A.B.; Grandini, C.R.; Afonso, C.R.M. Surface Characterization of New β Ti-25Ta-Zr-Nb Alloys Modified by Micro-Arc Oxidation. *Materials* **2023**, *16*, 2352. [[CrossRef](#)] [[PubMed](#)]
45. Dziaduszevska, M.; Shimabukuro, M.; Seramak, T.; Zielinski, A.; Hanawa, T. Effects of Micro-Arc Oxidation Process Parameters on Characteristics of Calcium-Phosphate Containing Oxide Layers on the Selective Laser Melted Ti₁₃Zr₁₃Nb Alloy. *Coatings* **2020**, *10*, 745. [[CrossRef](#)]
46. Molaiepour, P.; Allahkaram, S.R.; Akbarzadeh, S. Corrosion inhibition of Ti6Al4V alloy by a protective plasma electrolytic oxidation coating modified with boron carbide nanoparticles. *Surf. Coat. Technol.* **2022**, *430*, 127987. [[CrossRef](#)]
47. Wang, D.-d.; Liu, X.-t.; Wang, Y.; Zhang, Q.; Li, D.-l.; Liu, X.; Su, H.; Zhang, Y.; Yu, S.-x.; Shen, D. Role of the electrolyte composition in establishing plasma discharges and coating growth process during a micro-arc oxidation. *Surf. Coat. Technol.* **2020**, *402*, 126349. [[CrossRef](#)]
48. Halliday, D.; Resnick, R.; Walker, J. *Fundamentos de Física*, 10th ed.; Editora Livros Técnicos e Científicos (LTC): Rio de Janeiro, Brazil, 2016; Volume 3.
49. Duarte, L.T.; Bolfarini, C.; Biaggio, S.R.; Rocha-Filho, R.C.; Nascente, P.A.P. Growth of aluminum-free porous oxide layers on titanium and its alloys Ti-6Al-4V and Ti-6Al-7Nb by micro-arc oxidation. *Mater. Sci. Eng. C* **2014**, *41*, 343–348. [[CrossRef](#)]

50. Zhang, X.; Yu, Y.; Jiang, D.; Jiao, Y.; Wu, Y.; Peng, Z.; Zhou, J.; Wu, J.; Dong, Z. Synthesis and characterization of a bi-functional hydroxyapatite/Cu-doped TiO₂ composite coating. *Ceram. Int.* **2019**, *45*, 6693–6701. [[CrossRef](#)]
51. Zhang, L.; Guo, J.; Huang, X.; Zhang, Y.; Han, Y. The dual function of Cu-doped TiO₂ coatings on titanium for application in percutaneous implants. *J. Mater. Chem. B* **2016**, *4*, 3788–3800. [[CrossRef](#)]
52. Çaha, I.; Alves, A.C.; Affonço, L.J.; Lisboa-Filho, P.N.; da Silva, J.H.D.; Rocha, L.A.; Pinto, A.M.P.; Toptan, F. Corrosion and tribocorrosion behaviour of titanium nitride thin films grown on titanium under different deposition times. *Surf. Coat. Technol.* **2019**, *374*, 878–888. [[CrossRef](#)]
53. Zhu, W.; Zhang, Z.; Gu, B.; Sun, J.; Zhu, L. Biological Activity and Antibacterial Property of Nano-structured TiO₂ Coating Incorporated with Cu Prepared by Micro-arc Oxidation. *J. Mater. Sci. Technol.* **2013**, *29*, 237–244. [[CrossRef](#)]
54. Wang, S.; Deng, L.; Lv, Y.; Zhang, T.; Zhang, X.; Dong, Z.; Cai, G. Construction of antifouling Cu-modified TiO₂ coating via micro-arc oxidation: The influence of Cu content. *Surf. Coat. Technol.* **2023**, *454*, 129197. [[CrossRef](#)]
55. Kumari, P.; Saha, R.; Saikia, G.; Bhujel, A.; Choudhury, M.G.; Jagdale, P.; Paul, S. Synthesis of Mixed-Phase TiO₂–ZrO₂ Nanocomposite for Photocatalytic Wastewater Treatment. *Toxics* **2023**, *11*, 234. [[CrossRef](#)] [[PubMed](#)]
56. Costa, N.A.; Correa, D.R.N.; Lisboa-Filho, P.N.; Sousa, T.S.P.; Grandini, C.R.; Rocha, L.A. Influence of the molybdenum on characteristics of oxide films produced by micro-arc oxidation on Ti-15Zr-based alloys. *Surf. Coat. Technol.* **2021**, *408*, 126856. [[CrossRef](#)]
57. Leśniak-Ziółkowska, K.; Kazek-Kęsik, A.; Rokosz, K.; Raaen, S.; Stolarczyk, A.; Krok-Borkowicz, M.; Pamuła, E.; Gołda-Cępa, M.; Brzychczy-Włoch, M.; Simka, W. Electrochemical modification of the Ti-15Mo alloy surface in solutions containing ZnO and Zn₃(PO₄)₂ particles. *Mater. Sci. Eng. C* **2020**, *115*, 111098. [[CrossRef](#)] [[PubMed](#)]
58. Nie, X.; Cai, R.; Zhao, C.; Sun, J.; Zhang, J.; Matthews, D.T.A. Advancement of plasma electrolytic oxidation towards non-valve metals. *Surf. Coat. Technol.* **2022**, *442*, 128403. [[CrossRef](#)]
59. Cardoso, G.C.; Barbaro, K.; Kuroda, P.A.B.; Imperatori, L.; De Bonis, A.; Teghil, R.; Curcio, M.; Innocenzi, E.; Grigorieva, V.Y.; Vadalà, G.; et al. Incorporation of Ca, P, Mg, and Zn Elements in Ti-30Nb-5Mo Alloy by Micro-Arc Oxidation for Biomedical Implant Applications: Surface Characterization, Cellular Growth, and Microorganisms' Activity. *Coatings* **2023**, *13*, 1577.
60. Zhang, X.; Peng, Z.; Lu, X.; Lv, Y.; Cai, G.; Yang, L.; Dong, Z. Microstructural evolution and biological performance of Cu-incorporated TiO₂ coating fabricated through one-step micro-arc oxidation. *Appl. Surf. Sci.* **2020**, *508*, 144766. [[CrossRef](#)]
61. Yang, J.; Fang, K.; Xu, K.; Shen, X.; Xu, X. Effect of zinc or copper doping on corrosion resistance and anti-oxidative stress of strontium-based micro-arc oxidation coatings on titanium. *Appl. Surf. Sci.* **2023**, *626*, 157229. [[CrossRef](#)]
62. Kuroda, P.A.B.; de Mattos, F.N.; Grandini, C.R.; Afonso, C.R.M. Influence of the heat treatment temperature on the MAO coating produced in the Ti-25Ta-25Zr alloy. *J. Mater. Res. Technol.* **2023**, *26*, 3881–3892. [[CrossRef](#)]
63. Kuroda, P.A.B.; Rossi, M.C.; Grandini, C.R.; Afonso, C.R.M. Assessment of applied voltage on the structure, pore size, hardness, elastic modulus, and adhesion of anodic coatings in Ca-, P-, and Mg-rich produced by MAO in Ti-25Ta-Zr alloys. *J. Mater. Res. Technol.* **2023**, *26*, 4656–4669. [[CrossRef](#)]
64. Li, Y.; Wang, W.; Yu, F.; Wang, D.; Guan, S.; Li, Y.; Qi, M. Characterization and cytocompatibility of hierarchical porous TiO₂ coatings incorporated with calcium and strontium by one-step micro-arc oxidation. *Mater. Sci. Eng. C* **2020**, *109*, 110610. [[CrossRef](#)] [[PubMed](#)]
65. Karbowniczek, J.; Muhaffel, F.; Cempura, G.; Cimenoglu, H.; Czyska-Filemonowicz, A. Influence of electrolyte composition on microstructure, adhesion and bioactivity of micro-arc oxidation coatings produced on biomedical Ti6Al7Nb alloy. *Surf. Coat. Technol.* **2017**, *321*, 97–107. [[CrossRef](#)]
66. Yang, W.; Xu, D.; Guo, Q.; Chen, T.; Chen, J. Influence of electrolyte composition on microstructure and properties of coatings formed on pure Ti substrate by micro arc oxidation. *Surf. Coat. Technol.* **2018**, *349*, 522–528. [[CrossRef](#)]
67. Kuroda, P.A.B.; de Mattos, F.N.; Grandini, C.R.; Afonso, C.R.M. Effect of heat treatment on the phases, pore size, roughness, wettability, hardness, adhesion, and wear of Ti-25Ta MAO coatings for use as biomaterials. *J. Mater. Sci.* **2023**, *58*, 15485–15498. [[CrossRef](#)]
68. Li, G.; Ma, F.; Liu, P.; Qi, S.; Li, W.; Zhang, K.; Chen, X. Review of micro-arc oxidation of titanium alloys: Mechanism, properties and applications. *J. Alloys Compd.* **2023**, *948*, 169773. [[CrossRef](#)]
69. Raffi, M.; Mehrwan, S.; Bhatti, T.M.; Akhter, J.I.; Hameed, A.; Yawar, W.; ul Hasan, M.M. Investigations into the antibacterial behavior of copper nanoparticles against Escherichia coli. *Ann. Microbiol.* **2010**, *60*, 75–80. [[CrossRef](#)]
70. Cady, N.C.; Behnke, J.L.; Strickland, A.D. Copper-Based Nanostructured Coatings on Natural Cellulose: Nanocomposites Exhibiting Rapid and Efficient Inhibition of a Multi-Drug Resistant Wound Pathogen, *A. baumannii*, and Mammalian Cell Biocompatibility In Vitro. *Adv. Funct. Mater.* **2011**, *21*, 2506–2514. [[CrossRef](#)]
71. Shimabukuro, M.; Tsutsumi, Y.; Nozaki, K.; Chen, P.; Yamada, R.; Ashida, M.; Doi, H.; Nagai, A.; Hanawa, T. Investigation of antibacterial effect of copper introduced titanium surface by electrochemical treatment against facultative anaerobic bacteria. *Dent. Mater. J.* **2020**, *39*, 639–647. [[CrossRef](#)]
72. ISO 10993-5; Biological Evaluation of Medical Devices. Part 5: Test for Cytotoxicity: In Vitro Methods. International Organization for Standardization: Geneva, Sweden, 2005.
73. Chen, H.; Cheng, D.-H.; Huang, S.-C.; Lin, Y.-M. Comparison of flexural properties and cytotoxicity of interim materials printed from mono-LCD and DLP 3D printers. *J. Prosthet. Dent.* **2021**, *126*, 703–708. [[CrossRef](#)] [[PubMed](#)]

74. Jablonská, E.; Kubásek, J.; Vojtěch, D.; Ruml, T.; Lipov, J. Test conditions can significantly affect the results of in vitro cytotoxicity testing of degradable metallic biomaterials. *Sci. Rep.* **2021**, *11*, 6628. [[CrossRef](#)] [[PubMed](#)]
75. Srivastava, G.K.; Alonso-Alonso, M.L.; Fernandez-Bueno, I.; Garcia-Gutierrez, M.T.; Rull, F.; Medina, J.; Coco, R.M.; Pastor, J.C. Comparison between direct contact and extract exposure methods for PFO cytotoxicity evaluation. *Sci. Rep.* **2018**, *8*, 1425. [[CrossRef](#)] [[PubMed](#)]
76. Wang, K.; Tong, X.; Lin, J.; Wei, A.; Li, Y.; Dargusch, M.; Wen, C. Binary Zn–Ti alloys for orthopedic applications: Corrosion and degradation behaviors, friction and wear performance, and cytotoxicity. *J. Mater. Sci. Technol.* **2021**, *74*, 216–229. [[CrossRef](#)]

Disclaimer/Publisher’s Note: The statements, opinions and data contained in all publications are solely those of the individual author(s) and contributor(s) and not of MDPI and/or the editor(s). MDPI and/or the editor(s) disclaim responsibility for any injury to people or property resulting from any ideas, methods, instructions or products referred to in the content.